Electronic structure and the origin of the Dzyaloshinskii-Moriya interaction in MnSi

K. V. Shanavas*
Department of Physics, University of Missouri, Columbia, MO 65211, USA and
Materials Science and Technology Division, Oak Ridge National Laboratory, Oak Ridge, Tennessee 37831-6056, USA

S. Satpathy
Department of Physics, University of Missouri, Columbia, MO 65211, USA

The metallic helimagnet MnSi has been found to exhibit skyrmionic spin textures when subjected to magnetic fields at low temperatures. The Dzyaloshinskii-Moriya (DM) interaction plays a key role in stabilizing the skyrmion state. With the help of first-principles calculations, crystal field theory and a tight-binding model we study the electronic structure and the origin of the DM interaction in the B20 phase of MnSi. The strength of $\vec{D}$ parameter is determined by the magnitude of the spin-orbit interaction and the degree of orbital mixing, induced by the symmetry-breaking distortions in the B20 phase. Our calculations suggest strong coupling between Mn-d and Si-p states, which is consistent with a mixed valence ground state $|d^{7-x}p^{2+x}\rangle$ configuration. Consistent with previous calculations, we find that DFT+U leads to the experimental magnetic moment of $0.4\ \mu_B$, which redistributes electrons between the majority and minority spin channels. We derive the magnetic interaction parameters J and $\vec{D}$ for Mn-Si-Mn superexchange paths using Moriya's theory assuming the interaction to be mediated by e_g electrons near the Fermi level. Using parameters from our calculations, we get reasonable agreement with the observations.

PACS numbers: 12.39.Dc,31.15.A-,75.10.Dg,31.15.aq

I. INTRODUCTION

Recent observations of skyrmions [1] in magnetic solids have raised considerable interest in this new magnetic state. The skyrmion state is a novel, vortex-like spin structure that carries a characteristic topological charge S, which is $S = \pm 1$ for skyrmionic state and $S = 0$ for ferromagnetic and spin spiral states [2]. Materials with skyrmionic textures are anticipated to produce unconventional spin-electronic functions such as the topological Hall effect [3]. Experiments have confirmed their existence in chiral magnets with B20 crystal structures such as MnSi, MnGe, $Fe_{1-x}Co_xSi$ etc. when subjected to small magnetic fields [4, 5]. Competition between magnetic exchange, Dzyaloshinskii-Moriya (DM) interaction, and Zeeman coupling to the external magnetic field stabilizes this unique magnetic arrangement [6–8]. While the exchange coupling tries to align the spins parallel or antiparallel, the DM coupling tries align them perpendicular. It has the form $\vec{D} \cdot (\vec{S}_i \times \vec{S}_j)$, where $\vec{D}$ is the DM coupling parameter and $\vec{S}_i, \vec{S}_j$ are the spins at sites i, j. For the DM interaction to be present, in addition to strong spin-orbit coupling and magnetism, the system should have no inversion symmetry, making certain class of materials special [9, 10].

MnSi, which is a prime example of an itinerant magnet, develops a helical magnetic order below the transition temperature $T_c = 29.5$ K with a saturation magnetic moment of $0.4\ \mu_B$/Mn. Interestingly, the measured magnetic moment in this system is much lower than the value of $1.4\ \mu_B$/Mn calculated by the Curie-Weiss theory [11]. A mixed valence state of Mn-d orbitals [12] and spin fluctuations originating from Fermi surface nesting [13] are proposed as possible explanations for this discrepancy. The spin spiral has a large periodicity $\lambda_h \approx 180$ Å and is aligned along the cubic space diagonal $\langle 111 \rangle$. When a perpendicular magnetic field is applied to the thin films of MnSi just below the ordering temperature, a new magnetic phase (called the A-phase) develops, that exhibits skyrmionic textures [4].

Theoretical studies using density functional theory (DFT) incorrectly predicts a moment of $1.0\mu_B$/Mn [14] and application of Hubbard U has been found to lead to a low moment solution [8]. Exchange interactions in bulk and thin films of MnSi were studied in order to explain the ferromagnetism observed in thin films of MnSi/Si(100) [15]. Hopkinson *et al* considered the electrons in the magnetic ground state of MnSi to be of dual character [16]; leading to both the local moment and itinerant conduction electrons that mediate the magnetic interaction through RKKY type interaction [17]. More recently, using a classical spin model with DM terms [18] and symmetry analysis [19], components of DM vectors with respect to the crystal structure were determined.

In this manuscript, we present results of first principles calculations and construct an effective model Hamiltonian to understand the ground state configuration and DM interaction of MnSi. While it is possible to estimate magnetic interaction parameters using first principles methods [20], the model developed in Part III provides an intuitive picture of the underlying interactions and is complementary to such calculations. We start with the centrosymmetric FCC structure and analyze the changes brought about by the structural distortion. The DFT band structure is used to derive parameters for a tight-binding model, which are in turn used to construct a model for DM interaction in the solid.

II. FIRST PRINCIPLES CALCULATIONS

Calculations within density functional theory are performed using the Vienna ab-initio simulation package [21], within the projector augmented wave method. We use local density ap-

proximation with a plane wave energy cut-off of 500 eV and k-space sampling on a $12 \times 12 \times 12$ Monkhorst-Pack grid. All structural relaxations are carried out till Hellman-Feynman forces became less than 0.01 eV/Å. Effects of Hubbard U are studied with Coulomb-corrected DFT+U calculation using the all electron code WIEN2K [22] with the gradient corrected functional [23].

A. Crystal structure

MnSi crystallizes in the B20 phase [6], which has a cubic cell with a lattice constant of $a = 4.56$ Å and point group symmetry of $P2_13$. This phase can be understood by starting from the rock-salt FCC structure in which each Mn and Si atoms have six neighbors and equal bondlengths as shown in Fig. 1(a) with bond angles of 135°. A pairing type trigonal distortion along the body diagonal, in which successive MnSi units compress and elongate, leads to the B20 structure [24]. As a consequence, each Mn and Si atoms have seven neighbors and three types of bondlengths in B20 phase [25] as indicated in Fig. 1(d). The distortion also breaks inversion symmetry.

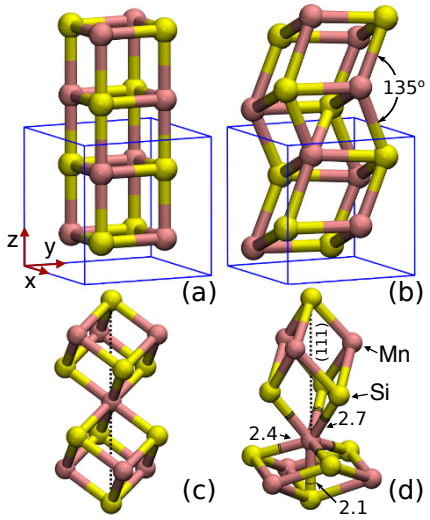

FIG. 1. Crystal structure of MnSi in (a) FCC and (b) B20 phases. The Mn and Si occupy equivalent positions. The unit cell is represented by the blue cube. Bonding along the (111) direction (dotted lines) in (c) FCC and (d) B20 structures are also shown. Three different kinds of bonds in B20 phase are marked in Angstrom. In the B20 structure, the Mn_4Si_4 cubes are alternately elongated and compressed along the (111) direction as indicated in (d).

Although the Bravais lattice remains simple cubic, the symmetry is reduced to four 3 fold axis in the FCC phase. Both Mn and Si atoms occupy the 4(a)-type sites with point group symmetry C_3, with position coordinates (u, u, u), $(\frac{1}{2}+u, \frac{1}{2}-u, \bar{u})$, $(\bar{u}, \frac{1}{2}+u, \frac{1}{2}-u)$, and $(\frac{1}{2}-u, \bar{u}, \frac{1}{2}+u)$. The internal atom-position parameters are $u_{Mn} = 0.137$ and $u_{Si} = 0.845$.

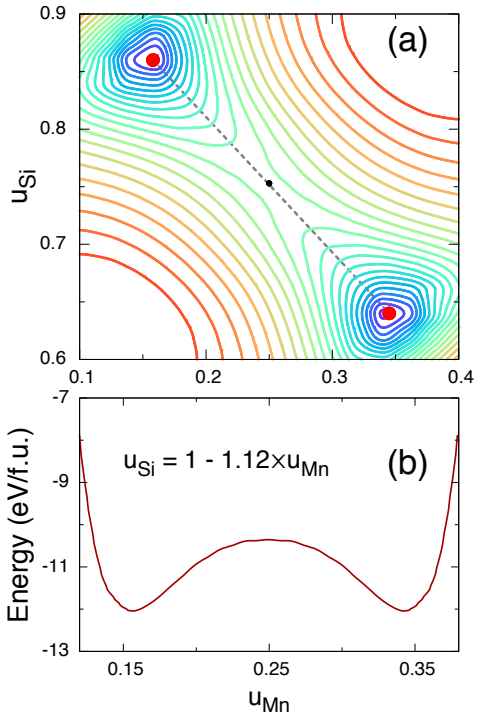

FIG. 2. (a) Contour plot of the total energy as a function of positional parameters u_{Mn} and u_{Si}. Endpoints of the line joining the two minima correspond to B20 structure while its center corresponds to FCC. (b) Variation of energy along the line connecting B20 structures.

Despite extensive studies, it is not clear from a local bonding picture, why MnSi and other transition metal monosilicides prefer the B20 structure. A Fermi surface nesting driven instability has been ruled out to be a factor, as several compounds with different band fillings exist in same structure [24]. The energy landscape of MnSi shown in Fig. 2, reveal that the FCC structure is metastable. For the range of u_{Mn} and u_{Si} studied, the two minima marked with circles correspond to B20 structure with parameters (0.16,0.86) and (0.34,0.64) related by a lattice translation. The FCC phase lies in between at (0.25, 0.75) and the three points can be joined by a straight line with a slope of $du_{\rm Si}/du_{\rm Mn} = -0.82$. Variation of energy along this line shows the familiar double well structure as shown in Fig. 2(b) with an energy difference of 1.94 eV per molecule which is in agreement with earlier studies [14].

B. Electronic structure of the FCC phase

To simplify the analysis of the electronic structure of MnSi, we start with that of the FCC phase. The primitive cell of FCC lattice contains two octahedrally coordinated atoms. The non-magnetic band structure along with the orbital character and symmetry properties is plotted in Fig. 3. In agreement with earlier studies, Si-s bands lie below -8 eV [14, 24]. The

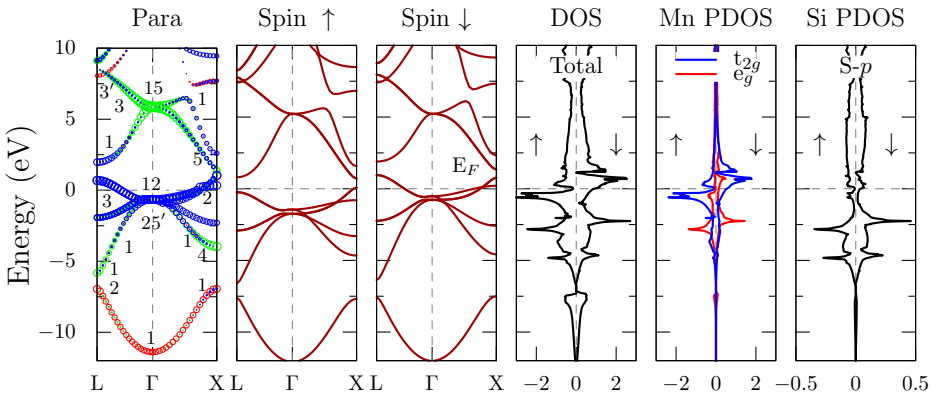

FIG. 3. DFT band structure and density of states for the FCC phase of MnSi. First panel shows non-magnetic band structure with orbital weights indicated by colored circles: red for Si-s, green for Si-p and blue for Mn-d. The numbers stand for the symmetry characters of the bands as listed in Table I. Second and third panel shows ferromagnetic band structures for spin and up and down channels and the corresponding total density of states is shown in the fourth panel. The partial density of states for Mn-t_{2g}, e_g and Si-p states are shown in last two panels.

TABLE I. Irreducible representations of the O_h^5 point group spanned by atom-centered orbitals in the MnSi FCC structure. Points Λ and Δ are the midpoints of $\Gamma - L$ and $\Gamma - X$ respectively.

	L	Λ	Γ	Δ	X
Mn-s	L_1	Λ_1	Γ_1	Δ_1	X_1
Mn-p	$L_{2'} + L_{3'}$	$\Lambda_1 + \Lambda_3$	Γ_{15}	$\Delta_1 + \Delta_5$	$X_{4'} + X_{5'}$
Mn-d	$L_1 + 2L_3$	$\Lambda_1 + 2\Lambda_3$	$\Gamma_{12} + \Gamma_{25'}$	$\Delta_1 + \Delta_2 + \Delta_{2'} + \Delta_5$	$X_1 + X_2 + X_3 + X_5$
Si-s	$L_{2'}$	Λ_1	Γ_1	Δ_1	X_1
Si-p	$L_1 + L_3$	$\Lambda_1 + \Lambda_3$	Γ_{15}	$\Delta_1 + \Delta_5$	$X_{4'} + X_{5'}$
Si-d	$L_{2'} + 2L_{3'}$	$\Lambda_1 + 2\Lambda_3$	$\Gamma_{12} + \Gamma_{25'}$	$\Delta_1 + \Delta_2 + \Delta_{2'} + \Delta_5$	$X_1 + X_2 + X_3 + X_5$

five bands close to the Fermi level at the Γ point originate from Mn-d, with hardly any splitting between the e_g ($3z^2 - r^2, x^2 - y^2$) and t_{2g} (xy, xz, yz) levels. Si-p bands couple strongly with d bands at generic k-points and split across -3 eV to -7 eV and 3 eV to 7 eV.

From the symmetry characters [26] marked in Fig 3 and listed in Table I, one can understand which bands are allowed to interact at the special points. It shows that $d - p$ orbital overlap is forbidden by symmetry only at Γ and X points. As a consequence, a singlet band in Γ_{15} manifold develops strong d character along $\Lambda_1 - L_3$ and $\Delta_5 - X_{5'}$ directions; while a singlet d band from $\Gamma_{25'}$ develops strong p character along $\Lambda_1 - L_1$ and $\Delta_1 - X_4$ directions, which indicate strong $d - p$ mixing along these directions, in agreement with electronic structure calculations. Detailed symmetry representations are given in Table I. Mn-s bands are absent from the band structure, indicating $s^0 d^7$ configuration for Mn and $s^2 p^2$ for Si. Calculated Bader charges using optimized charge densities also confirm this picture.

Spin polarized density of states (DOS) in Fig. 3 shows that there is a small exchange splitting of the order of 1 eV in the FCC phase. The effect of crystal field is much larger, at about 3 eV. Since the splitting at Γ point is negligible, this indicates that the crystal field potential is highly k dependent. Comparing the band structure and partial DOS shows that most of the contribution to the peaks in density comes from states that are close to the zone boundary.

To estimate strengths of orbital overlaps, we constructed a tight-binding model with five Mn-d and three Si-p atomic orbitals as basis [27, 28]. Nearest neighbor Mn-Mn, Mn-Si and Si-Si electronic hopping matrix elements are included. We used the DFT non-magnetic band structure in Fig. 3 to fit the parameters of this 8×8 model Hamiltonian, which yield, the onsite energies (in eV) $\epsilon(e_g) = -1.4, \epsilon(t_{2g}) = -0.8$, $\epsilon_p = 1.5$, and hopping parameters, $V_{dd\sigma} = -0.35$, $V_{dd\pi} = 0.15$, $V_{pp\sigma} = 1.3$, $V_{pp\pi} = -0.15$, $V_{pd\sigma} = 1.0$ and $V_{pd\sigma} = -0.9$.

C. Electronic structure of the B20 phase

As a consequence of the B20 distortion, the primitive cell becomes same as the conventional cell with four formula units (f.u.) and the electronic structure becomes more complex with four times the number of bands. Still, several interesting features can be observed in the band dispersions shown in Fig 4. Firstly, the reduced symmetry in the B20 phase lifts the degeneracy of bands at generic k-points, however, around R the bands are similar to the FCC phase, as the three fold axis along (111) is preserved after the distortion. The Mn-d bands form three groups with the lower group of eight bands having predominant e_g character, middle group of eight bands and top four bands with t_{2g} character. Another effect of distortion is

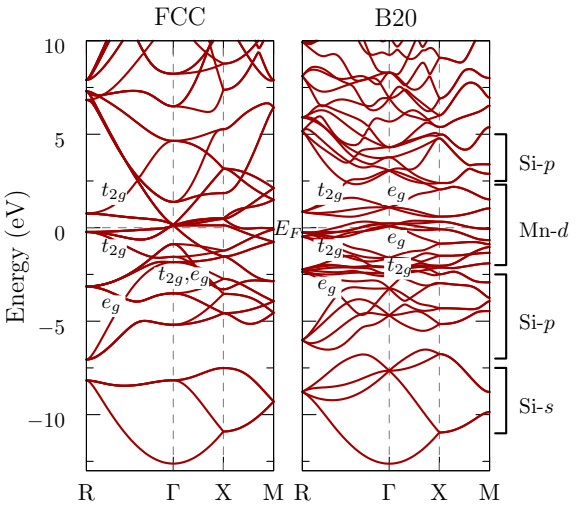

FIG. 4. The bands of non-magnetic MnSi in FCC (left) and B20 (right) phases in the four-molecule unit cell. Fermi energy is located at 0 eV. The labels mark dominant band character.

opening of a narrow gap between the top four bands and the rest of Mn d bands, just above the Fermi level. In FeSi, which has four more electrons per unitcell than MnSi, this gap leads to semiconducting behavior for both spin channels [24]. Spin polarized band structure and partial density of states of MnSi in the B20 structure are given in Fig 5. Four bands above Fermi level has dominant Mn-d character indicating that one hole (per Mn atom) exists in the up-spin channel and while two holes exist in the down-spin channel. The narrow gap just above the Fermi level in the spin-up channel leads to a half metallic density of states, resulting in an integer magnetic moment of 1 μ_B.

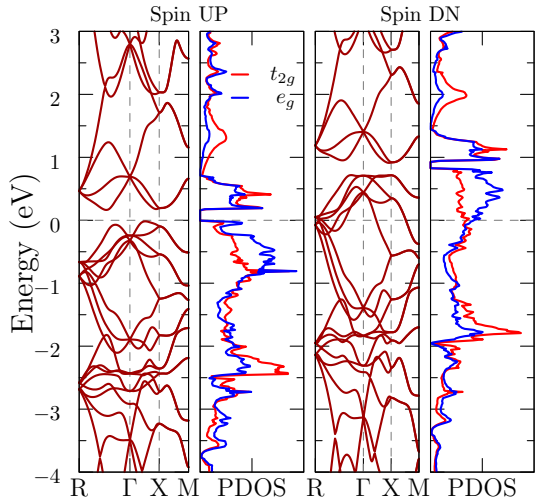

FIG. 5. Spin polarized band structure and partial density of states in the B20 phase of MnSi. In the partial DOS, blue and red lines correspond to e_g and t_{2g} states respectively.

Partial DOS shows substantial contributions from both e_g and t_{2g} characters across the entire energy range of d states -3 to 1 eV, indicating that there is strong mixing between the states. Since B20 distortion is a modified trigonal field with alternate elongation and compression of the MnSi cubes along the (111) direction, we arrive at the level diagram shown in Fig. 6, where the cubic crystal field in the FCC structure splits the d states into doubly degenerate e_g and triply-degenerate t_{2g} states. The trigonal distortion splits the t_{2g} levels further into a doublet ($t_\pm$) and a singlet (t_0). A convenient form for these states were proposed by Pryce and Runciman, viz., [29, 30]

$$
\begin{aligned}
t_0 &= \frac{1}{\sqrt{3}}[(xy)+(yz)+(xz)] \\
t_+ &= -\frac{1}{\sqrt{3}}[(xy)+\omega(yz)+\omega^2(xz)] \\
t_- &= \frac{1}{\sqrt{3}}[(xy)+\omega^{-1}(yz)+\omega^{-2}(xz)] \\
e_+ &= -\frac{1}{\sqrt{2}}[(3z^2-r^2)+i\sqrt{3}(x^2-y^2)] \\
e_- &= \frac{1}{\sqrt{2}}[(3z^2-r^2)-i\sqrt{3}(x^2-y^2)], \qquad (1)
\end{aligned}
$$

where $\omega = e^{2i\pi/3}$. Actually, a small but nonzero mixing between $t_\pm$ and $e_\pm$ exists in the trigonal structure [30], but it affects the t_+/e_+ and the t_-/e_- states equally, so that the double-degeneracies (Fig. 6) in the trigonal structure are not broken. The B20 distortion removes all degeneracies of d orbitals as indicated in Fig. 6. The "e_g" hole at the Fermi energy has minority spin character with a strong admixture of the t_{2g} orbitals, but as seen from the DOS, Fig. 5, the e_g character is dominant for both the majority-spin electron as well as the minority-spin hole, leading to the simplified level structure presented in Fig. 6.

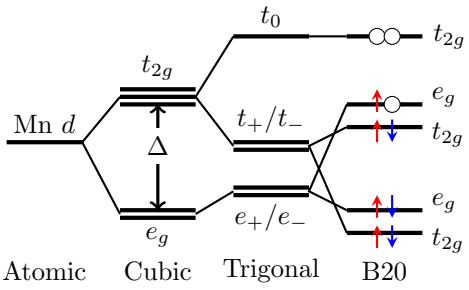

FIG. 6. Level splitting for Mn d states in MnSi, as inferred from the DFT results, Figs. 4 and 5. In the trigonal distortion, the structure is expanded (or compressed) uniformly along the cube diagonal direction (111), while in the B20 structure, the cubes are alternately compressed and expanded along the same direction (see Fig. 1). The "e_g/t_{2g}" characters for the B20 structure indicated on right shows the approximate character of the orbitals, referring to the cubic basis.

The electronic configuration inferred from the band structure above is: $p^1_\uparrow e^2_{g\uparrow} t^2_{2g\uparrow}$ and $p^1_\downarrow e^1_{g\downarrow} t^2_{2g\downarrow}$, which leads to a $|d^7p^2\rangle$ nominal configuration and a net magnetic moment of

$1\mu_B$ in the DFT calculations. However, the band counting shows *only* that there are five electrons per MnSi formula unit in the spin up channel, contributed from Mn-d and Si-p, while it is four such electrons in the spin down channel. Since there is strong mixture of Si-p and Mn-d orbitals and they form a joint band, it is difficult to infer the number of electrons in the p and d orbitals, and a configuration like $p_\uparrow^{1+x}(e_{g\uparrow}t_{2g\uparrow})^{4-x}$ and $p_\downarrow^{1+y}(e_{g\downarrow}t_{2g\downarrow})^{3-y}$, where x and y are fractions of one, is consistent with the band structure. This is especially so, since it is impossible to partition charges between atoms in a solid in a unique manner. This all fits together with the mixed valence nature of the Mn ion, viz., d^6 and d^7, derived from the x-ray absorption data [12]. Such spin fluctuation has also been suggested from recent ARPES measurements that indicate a nested Fermi surface [13].

Coulomb corrected GGA+U results – We note that, in spite of the difficulty of partitioning the charges among the atoms as discussed above, the net magnetic moment per unit cell is still 1 μ_B (the integer number coming from the half-metallic band structure), while the experimental value is 0.4 μ_B. Our Coulomb-corrected DFT+U calculations show that the Mn-d charge remains more-or-less the same irrespective of the strength of the U value used. This is because the Fermi energy falls in the manifold of the Mn-d states with the Si-p states lying far away in energy, so that it is energetically unfavorable to move electrons between these orbitals. However, there is a shift of charge between the spin up and spin down channels and, unlike the DFT results, the bands are no longer half-metallic, which yields a net magnetic moment less than 1 μ_B. The actual value depends on the magnitude of the Hubbard U and the calculated spin moment agree with the measured value of 0.4 μ_B for $U \approx 6$ eV, which is a reasonable value for the on-site Coulomb repulsion for the $3d$ electrons and consistent with the earlier DFT+U calculations [8].

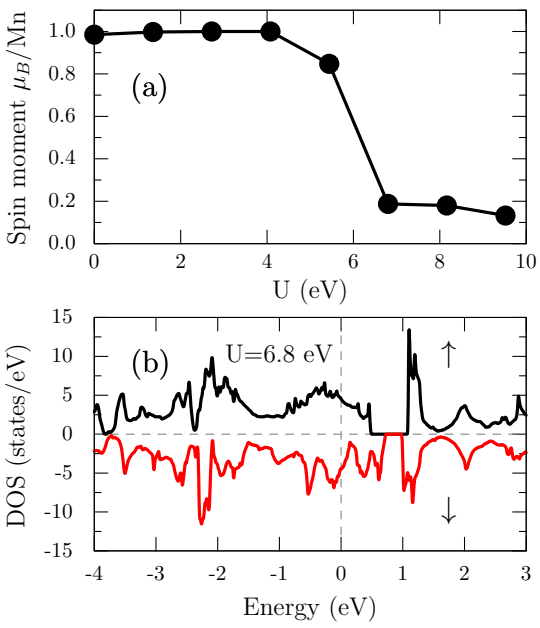

FIG. 7. Effect of Hubbard parameter U on the (a) magnetic moment and (b) density of states of the B20 phase from GGA+U calculations. Spin of Mn ions remain close to 1 μ_B till $U = 4$ eV and drops to 0.2 μ_B above 6 eV. The DOS is calculated for $U = 6.8$ eV.

III. DZYALOSHINSKII-MORIYA INTERACTION

In this section, we turn our attention to the magnetic interactions between the Mn moments. The helical spin structure that develops at low temperatures and transforms to the skyrmionic state upon application of a magnetic field [4] is known to arise from the interplay of Heisenberg exchange and DM interactions. Here, we examine the origin of these interactions based on a simplified model Hamiltonian, extracted from the density-functional results. For simplicity, in the following we derive the magnetic interaction between two Mn spins interconnected through the Si-p states shown in Fig. 8. Downfolding the Hamiltonian into an effective ground state model using perturbation theory, we can derive the parameters J and $\vec{D}$ for the above pair.

It is well known that in the weak coupling limit [31], a two site, two particle Hubbard model with hopping parameter t and Coulomb repulsion U, can be reduced to the Heisenberg form $H_{\rm eff} = J\,\mathbf{S}_1 \cdot \mathbf{S}_2$, where the exchange coupling is given by $J = 4t^2/U$. In the case of superexchange [32], where the interaction takes place through an intermediate site (such as in MnSi), the result is $J = 4gt^4$, where

$$g = \frac{1}{\Delta^2}\left[\frac{1}{U} + \frac{1}{\Delta}\right] \tag{2}$$

and $\Delta = \varepsilon_p - \varepsilon_d$ is the bare charge transfer energy from Mn-d to Si-p states. Further, when spin-orbit coupling is present and inversion symmetry is absent, the transformation yields additional terms such as $\vec{D} \cdot \vec{S}_1 \times \vec{S}_2$, where $\vec{D}$ is the Dzyaloshinskii vector [9]. To estimate the strength of D in MnSi, we consider a typical Mn-Si-Mn bond shown in Fig. 8, in which the inversion symmetry at the midpoint of the line connecting two Mn atoms is broken by the bend through angle θ. For this three site model, we write the Hamiltonian as $H = H_0^d + H_0^p + H_t + H_{SO}$, where

$$\begin{aligned}
H_0^d &= \sum_{jm\sigma} \epsilon_m^d d_{jm\sigma}^\dagger d_{jm\sigma} + U \sum_{jm\sigma,m'\sigma'} n_{jm\sigma} n_{jm'\sigma'} \\
H_0^p &= \sum_{k\sigma} \epsilon^p p_{k\sigma}^\dagger p_{k\sigma} \\
H_t &= \sum_{jmk\sigma} V_{jmk}\, d_{jm\sigma}^\dagger p_{k\sigma} + h.c. \\
H_{SO} &= \lambda \sum_j \vec{L}_j \cdot \vec{S}_j .
\end{aligned} \tag{3}$$

The sum j runs over the two Mn sites, A and B, m and k run over the five Mn-d and the three Si-p orbitals, respectively, and the sum σ runs over the two spins. Here, H_0^d and H_0^p are onsite terms for d and p sites respectively, H_t is the Mn-Si interaction Hamiltonian, and H_{SO} is the spin-orbit coupling

within the d states. The onsite energies are ϵ^d_m and ϵ^p, U is the Coulomb repulsion for the d orbitals, and V_{jmk} are the hopping amplitudes between the Mn d_m on the j-th site and Si p_k orbitals. In the ideal B20 structure with $u_{Mn} = 1/(4\tau)$ and $u_{Si} = 1 - 1/(4\tau)$ where $\tau = (1+\sqrt{5})/2$. This makes all Mn-Si bond lengths equal to $a\sqrt{3}/(2\pi)$ and all relevant Mn-Si-Mn bond angles equal to 138.19° simplifying the analysis.

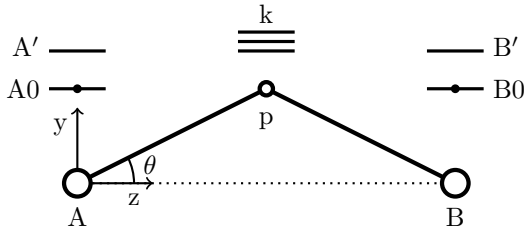

FIG. 8. A typical superexchange path between two Mn atoms through an intermediate Si atom. Interaction is mediated by the hopping of the two electrons indicated by the black dots occupying the orbitals A0 and B0. A′ and B′ are the remaining four d orbitals on each Mn (other than A0 and B0).

In our simplified model for MnSi, we consider the exchange interaction to be mediated by the single Mn "e_g" electron at the Fermi energy (Fig. 6), residing on the A0/B0 orbital (Fig. 8). The farther away an electron is from the Fermi energy, the less effective it is in mediating the exchange interaction, thus in our description only the electron closest to the Fermi energy is kept. Moriya showed that treating spin-orbit coupling as perturbation, H_{SO} and H_t can be combined to an effective hopping Hamiltonian [10] which allows "spin-flip" hopping between Mn-d and Si-p states through parameters $\vec{C}_{jk}$:

$$H_I = \sum_{j=A,B} \sum_{k,\sigma\sigma'} \left[V_{j0,k}\delta_{\sigma\sigma'} + \vec{C}_{jk} \cdot \vec{\tau}_{\sigma\sigma'} \right] d^\dagger_{j0,\sigma} p_{k,\sigma'} + h.c., \tag{4}$$

where $j0$ corresponds to the electron A0/B0, $\vec{\tau}_{\sigma\sigma'}$ are the Pauli matrices, and,

$$\vec{C}_{jk} = -\frac{\lambda}{2\epsilon_d} \sum_m{}' \vec{L}_{j,0m} V_{jm,k}, \tag{5}$$

where the prime indicates summation over the A′ or the B′ orbitals, ϵ_d is the energy difference between A0/B0 and other d states, $\vec{L}_{j,0m}$ are the matrix elements of the orbital angular momentum operator between A0/B0 state and the remaining four d states at the j-th site, and $\vec{C}_{kj} = \vec{C}^*_{kj}$. It is now straight forward [33] to downfold the Hamiltonian into an effective magnetic interaction between the Mn moments, with the help of fourth order perturbation theory:

$$H_{\text{eff}} = J\, \vec{S_A} \cdot \vec{S_B} + \vec{D} \cdot \vec{S}_A \times \vec{S}_B \tag{6}$$

where J and $\vec{D}$ are given by,

$$\begin{aligned} J &= 4g \sum_{kk'} V_{A0,k} V_{k,B0} V_{B0,k'} V_{k',A0} \\ \vec{D} &= 8ig \sum_{kk'} V_{A0,k} V_{k,B0} \left[\vec{C}_{B,k'} V_{k',A0} + V_{B0,k'} \vec{C}_{k',A} \right]. \end{aligned} \tag{7}$$

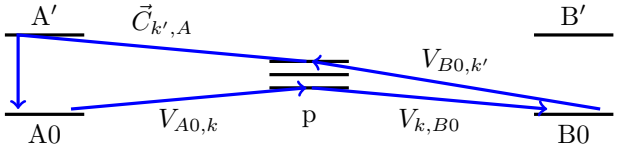

FIG. 9. One of the superexchange paths from Mn(A) to Mn(B) through an intermediate Si that leads to the DM vector $\vec{D}$. If the spin-flip hopping term $\vec{C}_{k',A}$ is replaced by standard hopping $V_{k',A0}$, then the interaction leads to the Heisenberg interaction J.

The remaining task is to evaluate the expressions Eq. (7) for the present case. Since the e_g electron has equal characters from the DFT calculations, we will consider the A0/B0 electronic wave function to be a linear combination $|A0\rangle = |B0\rangle = \alpha_1|3z^2 - r^2\rangle + \alpha_2|x^2 - y^2\rangle$ and take $|\alpha_1|^2 = |\alpha_2|^2 = 1/2$. Now, the hopping integrals also become linear combinations, $V_{A0,k} = \sum_l \alpha^*_l V_{l,k}$, where l runs over $3z^2 - r^2$ and $x^2 - y^2$, so that Eq. (7) immediately yields the result for J,

$$J = 4g \sum_{kk'} \sum_{lmno} \alpha^*_l \alpha_m \alpha^*_n \alpha_o V_{l,k} V_{k,m} V_{n,k'} V_{k',o}. \tag{8}$$

TABLE II. The hopping parameters V and $\vec{C}$ for Mn-Si-Mn model depicted in Fig. 8. Here $V'_{pd\sigma} \equiv V_{pd\sigma}/2\epsilon_d$, $V'_{pd\pi} \equiv V_{pd\pi}/2\epsilon_d$, and only leading terms in angle θ are kept.

$A = 3z^2 - r^2$		$B = 3z^2 - r^2$	
$V_{A0,x}$	0	$V_{B0,x}$	0
$V_{A0,y}$	$(\sqrt{3}V_{pd\pi} - V_{pd\sigma})\theta$	$V_{B0,y}$	$(\sqrt{3}V_{pd\pi} - V_{pd\sigma})\theta$
$V_{A0,z}$	$-V_{pd\sigma}$	$V_{B0,z}$	$V_{pd\sigma}$
$\vec{C}_{x,A}$	$-i\sqrt{3}\lambda V'_{pd\pi}\hat{y}$	$\vec{C}_{B,x}$	$-i\sqrt{3}\lambda V'_{pd\pi}\hat{y}$
$\vec{C}_{y,A}$	$i\sqrt{3}\lambda V'_{pd\pi}\hat{x}$	$\vec{C}_{B,y}$	$i\sqrt{3}\lambda V'_{pd\pi}\hat{x}$
$\vec{C}_{z,A}$	$-i\lambda(\sqrt{3}V'_{pd\pi} - 3V'_{pd\sigma})\theta\hat{x}$	$\vec{C}_{B,z}$	$i\lambda(\sqrt{3}V'_{pd\pi} - 3V'_{pd\sigma})\theta\hat{x}$
$A = x^2 - y^2$		$B = x^2 - y^2$	
$V_{A0,x}$	0	$V_{B0,x}$	0
$V_{A0,y}$	$V_{pd\pi}\theta$	$V_{B0,y}$	$V_{pd\pi}\theta$
$V_{A0,z}$	$(-V_{pd\pi} + \sqrt{3}V_{pd\sigma}/2)\theta^2$	$V_{B0,z}$	$(V_{pd\pi} - \sqrt{3}V_{pd\sigma}/2)\theta^2$
$\vec{C}_{x,A}$	$i\lambda V'_{pd\pi}\hat{y}$	$\vec{C}_{B,x}$	$i\lambda V'_{pd\pi}\hat{y}$
$\vec{C}_{y,A}$	$i\lambda V'_{pd\pi}\hat{x}$	$\vec{C}_{B,y}$	$i\lambda V'_{pd\pi}\hat{x}$
$\vec{C}_{z,A}$	$-i\lambda(V'_{pd\pi} - \sqrt{3}V'_{pd\sigma})\theta\hat{x}$	$\vec{C}_{B,z}$	$i\lambda(V'_{pd\pi} - \sqrt{3}V'_{pd\sigma})\theta\hat{x}$

The hopping matrix elements are easily evaluated using the Harrison's Tables, which are listed in Table. II for small θ, which is about 20° in MnSi. Plugging these in Eq. 8, we find

$$J = 4g|\alpha_1|^4 V^4_{pd\sigma} + O(\theta). \tag{9}$$

To calculate the DM vector, we need to evaluate the matrix elements of orbital moment vector $\vec{L}$, which is given in the cubic basis $\{3z^2-r^2, x^2-y^2, xy, xz, yz\}$ as:

$$\vec{L} = i \begin{pmatrix} 0 & 0 & 0 & -\sqrt{3}\hat{y} & \sqrt{3}\hat{x} \\ 0 & 0 & -2\hat{z} & \hat{y} & \hat{x} \\ 0 & 2\hat{z} & 0 & -\hat{x} & \hat{y} \\ \sqrt{3}\hat{y} & -\hat{y} & \hat{x} & 0 & -\hat{z} \\ -\sqrt{3}\hat{x} & -\hat{x} & -\hat{y} & \hat{z} & 0 \end{pmatrix}. \quad (10)$$

The calculated effective spin-flip hopping parameters $\vec{C}$ [using Eq. (5)] are also listed in Table. II. Again, we have the identity $\vec{C}_{j,k} = \vec{C}^*_{k,j}$ where $j = A, B$. A close inspection of the Table II and Eq. 7 shows that the dominant term in $\vec{D}$ is linear in θ and originates from the coupling of $3z^2 - r^2$ orbitals through the p_z orbitals of the intermediate site. Keeping the leading terms in the angle θ, the result is

$$\vec{D} = \frac{8g|\alpha_1|^4\lambda}{\epsilon_d} V^2_{pd\sigma}(3V^2_{pd\pi} - 2\sqrt{3}V_{pd\pi}V_{pd\sigma} + 3V^2_{pd\sigma})\theta\hat{x}. \quad (11)$$

As expected, the ratio, $D/J \sim O(\lambda/\epsilon_d)$, is proportional to the spin-orbit coupling strength. As pointed out by Moriya [10], the DM vector must also obey certain symmetry properties in the crystal, such as being perpendicular to the plane containing the bonds. Thus, the axial vector $\vec{D}$ lies in the direction of $\vec{r}_{Ap} \times \vec{r}_{AB}$, where $\vec{r}_{Ap}$ and $\vec{r}_{AB}$ are vectors connecting Mn(A) with Si and Mn(B) respectively [34]. Thus, for the superexchange path shown in Fig 8, $\vec{D}$ is along $\hat{x}$ in agreement with Moriya's symmetry rules. For all bonds in the ideal B20 structure $\vec{D}$ has same magnitude and points perpendicular to the plane containing the two Mn-Si bonds. (In the real structure, the Mn-Si-Mn bond angles are somewhat different between different triads, leading to slightly different strengths of $\vec{D}$.) Note that between any two given Mn spins, $\vec{D}$ can be zero, if there are two symmetric superexchange paths such that there is an inversion symmetry at the center of the line joining the two spins.

As expected, the exchange coupling J has a term independent of θ, while the lowest order term in $\vec{D}$ is linearly dependent on θ. This confirms that when inversion symmetry is present ($\theta = 0$) we will have a finite exchange coupling but no DM coupling. We can estimate the magnitudes of J and D using typical parameters obtained from the tight-binding calculations: $\Delta \approx 3$ eV, $U \approx 6$ eV, $V_{pd\sigma} \approx 1$ eV, $V_{pd\pi} \approx -0.9$ eV, $\lambda = 0.037$ eV for the atom [35, 36], $\epsilon_d \approx 2$ eV, and $\theta \approx 20^\circ$ leads to the numerical values: $J \approx 55$ meV and $D \approx 6.1$ meV, so that the ratio $D/J \approx 0.12$. The helical structure in MnSi is 180 Å long which is approximately 40 unitcells, which suggest $k = D/J = 2\pi/40 \sim 0.16$ [37]. Considering the crudeness of our model, the agreement with the experiments is reasonable.

IV. SUMMARY

Using first-principles and tight-binding methods, we studied the skyrmion compound MnSi both in the B20 and the ideal, rock salt structure in order to gain insight into the electronic structure and the origin of the Dzyaloshinskii-Moriya interaction. The B20 structure is formed by the alternate elongation and compression of the ideal MnSi cubes along the (111) direction, which breaks the inversion symmetry leading to the DM interaction. In both structures, strong coupling between Mn-d and Si-p indicate a mixed valence $|d^7p^2\rangle + |d^6p^3\rangle$ state, as suggested by the x-ray absorption data. The density-functional calculations show a half-metallic band structure, which leads to an integer magnetic moment 1 μ_B per Mn ion. However, the Coulomb-corrected GGA+U calculations redistributes the electrons between the majority and minority spin channels, and for $U \approx 6$ eV, the calculated magnetic moment drops close to the experimental value of 0.4 μ_B. We derived expressions for the exchange and DM interaction between the Mn atoms using a three-site model and find that the leading term in J is independent of the bond angle θ, but depends on the fourth power of orbital overlap $V_{pd\sigma}$. The magnitude of the DM interaction $\vec{D}$, however, depends linearly on both the bond angle θ as well as the spin-orbit coupling parameter λ, which leads to a vanishing $\vec{D}$ in the cubic phase, as expected. Our results provide insight into the electronic structure of the B20 phase and will hopefully lead to a deeper understanding of the skyrmion phase observed in this structure.

V. ACKNOWLEDGMENTS

We would like to thank Zoran Popović for stimulating discussions. The work at MU was supported by the US Department of Energy through Grant No. DE-FG02-00ER45818 and the work at ORNL was supported by the Critical Materials Institute, an Energy Innovation Hub funded by the U.S. Department of Energy, Energy Efficiency and Renewable Energy, Advanced Manufacturing Office.

* kavungalvees@ornl.gov

[1] T. H. R. Skyrme, "A unified field theory of mesons and baryons," Nuclear Physics **31**, 556 (1962).

[2] N. Romming, C. Hanneken, M. Menzel, J. E. Bickel, B. Wolter, K. von Bergmann, A. Kubetzka, and R. Wiesendanger, "Writing and deleting single magnetic skyrmions," Science **341**, 636 (2013).

[3] J. Gayles, F. Freimuth, T. Schena, G. Lani, P. Mavropoulos, R. A. Duine, S. Blügel, J. Sinova, and Y. Mokrousov, "Dzyaloshinskii-Moriya interaction and hall effects in the skyrmion phase of $Mn_{1-x}Fe_xGe$," Phys. Rev. Lett. **115**, 036602 (2015).

[4] S. Mühlbauer, B. Binz, F. Jonietz, C. Pfleiderer, A. Rosch, A. Neubauer, R. Georgii, and P. Boni, "Skyrmion lattice in a chiral magnet," Science **323**, 915 (2009).

[5] X. Z. Yu, N. Kanazawa, Y. Onose, K. Kimoto, W. Z. Zhang, S. Ishiwata, Y. Matsui, and Y. Tokura, "Near room-temperature formation of a skyrmion crystal in thin-films of the helimagnet FeGe," Nat. Mater. **10**, 106 (2011).

[6] O. Nakanishi, A. Yanase, and A. Hasegawa, "Electronic energy band structure of MnSi," J. Magn. Magn. Mater. **15-18**, 879 (1980).

[7] P. Bak and M. H. Jensen, "Theory of helical magnetic structures and phase transitions in MnSi and FeGe," J. Phys. C **13**, L881 (1980).

[8] R. D. Collyer and D. A. Browne, "Correlations and the magnetic moment of MnSi," Physica B **403**, 1420 (2008).

[9] I. Dzyaloshinsky, "A thermodynamic theory of "weak" ferromagnetism of antiferromagnetics," J. Phys. Chem. Solids **4**, 241 (1958).

[10] T. Moriya, "Anisotropic superexchange interaction and weak ferromagnetism," Phys. Rev. **120**, 91 (1960).

[11] Y. Ishikawa, G. Shirane, J. A. Tarvin, and M. Kohgi, "Magnetic excitations in the weak itinerant ferromagnet MnSi," Phys. Rev. B **16**, 4956–4970 (1977).

[12] F. Carbone, M. Zangrando, A. Brinkman, A. Nicolaou, F. Bondino, E. Magnano, A. A. Nugroho, F. Parmigiani, T. Jarlborg, and D. van der Marel, "Electronic structure of MnSi: The role of electron-electron interactions," Phys. Rev. B **73**, 085114 (2006).

[13] A. Nicolaou, M. Gatti, E. Magnano, P. Le Fèvre, F. Bondino, F. Bertran, A. Tejeda, M. Sauvage-Simkin, A. Vlad, Y. Garreau, A. Coati, N. Guérin, F. Parmigiani, and A. Taleb-Ibrahimi, "Fermi surface symmetry and evolution of the electronic structure across the paramagnetic-helimagnetic transition in MnSi/Si(111)," Phys. Rev. B **92**, 081110 (2015).

[14] T. Jeong and W. E. Pickett, "Implications of the B20 crystal structure for the magnetoelectronic structure of mnsi," Phys. Rev. B **70**, 075114 (2004).

[15] M. Hortamani, L. Sandratskii, P. Kratzer, I. Mertig, and M. Scheffler, "Exchange interactions and critical temperature of bulk and thin films of MnSi: A density functional theory study," Phys. Rev. B **78**, 104402 (2008).

[16] J. M. Hopkinson and H. Y. Kee, "Origin and consequences of unpinned helical order: Application to MnSi under pressure," Phys. Rev. B **79**, 014421 (2009).

[17] A. Fert and P. M. Levy, "Role of anisotropic exchange interactions in determining the properties of spin-glasses," Phys. Rev. Lett. **44**, 1538–1541 (1980).

[18] V. A. Chizhikov and V. E. Dmitrienko, "Frustrated magnetic helices in MnSi-type crystals," Phys. Rev. B **85**, 014421 (2012).

[19] V. E. Dmitrienko and V. A. Chizhikov, "Weak antiferromagnetic ordering induced by dzyaloshinskii-moriya interaction and pure magnetic reflections in MnSi-type crystals," Physical Review Letters **108**, 187203 (2012).

[20] A. N. Rudenko, V. V. Mazurenko, V. I. Anisimov, and A. I. Lichtenstein, "Weak ferromagnetism in Mn nanochains on the CuN surface," Phys. Rev. B **79**, 144418 (2009).

[21] G. Kresse and J. Hafner, "Ab initio molecular dynamics for liquid metals," Phys. Rev. B **47**, 558–561 (1993); G. Kresse and J. Furthmüller, "Efficient iterative schemes for ab initio total-energy calculations using a plane-wave basis set," *ibid*. **54**, 11169–11186 (1996).

[22] P. Blaha, K. Schwarz, G. K. H Madsen, D. Kvasnicka, and J. Luitz, *WIEN2k, An Augmented PlaneWave + Local Orbitals Program for Calculating Crystal Properties* (Karlheinz Schwarz, Techn. Universität Wien, Austria, 2001).

[23] John P. Perdew, Kieron Burke, and Matthias Ernzerhof, "Generalized gradient approximation made simple," Phys. Rev. Lett. **77**, 3865 (1996).

[24] L. F. Mattheiss and D. R. Hamann, "Band structure and semiconducting properties of FeSi," Phys. Rev. B **47**, 13114–13119 (1993).

[25] V. E. Dmitrienko, "Quasicrystals and their approximants: dodecahedral local ordering versus canonical-cell description," Acta Cryst A **50**, 515 (1994).

[26] L. Bouckaert, R. Smoluchowski, and E. Wigner, "Theory of brillouin zones and symmetry properties of wave functions in crystals," Phys. Rev. **50**, 58 (1936).

[27] W. A. Harrison, *Electronic Structure and the Properties of Solids: The Physics of the Chemical Bond* (Freeman, San Francisco, 1980).

[28] D. A. Papaconstantopoulos, *Handbook of the Band Structure of Elemental Solids* (Plenum Press, New York, 1986).

[29] M. H. L. Pryce and W. A. Runciman, "The absorption spectrum of vanadium corundum," Disc. Faraday Soc. **26**, 34 (1958).

[30] C. J. Ballhausen, *Introduction to ligand field theory* (McGraw-Hill, New York, 1962).

[31] P. W. Anderson, "New approach to the theory of superexchange interactions," Phys. Rev. **115**, 2 (1959).

[32] J. H. Jefferson, "Theory of superexchange in antiferromagnetic insulators," J. Phys. C **21**, L193 (1988).

[33] V. Yushankhai, M. Wolf, K.-H. Müller, R. Hayn, and H. Rosner, "Weak antiferromagnetism due to dzyaloshinskii-moriya interaction in $Ba_3Cu_2O_4Cl_2$," Phys. Rev. B **62**, 14229–14236 (2000).

[34] F. Keffer, "Moriya interaction and the problem of the spin arrangements in β-MnS," Phys. Rev. **126**, 896 (1962).

[35] F. Herman and S. Skillman, *Atomic Structure Calculations* (Prentice-Hall, New Jersey, 1963).

[36] K. V. Shanavas, Z. S. Popović, and S. Satpathy, "Theoretical model for rashba spin-orbit interaction in d electrons," Phys. Rev. B **90**, 165108 (2014).

[37] S. V. Grigoriev, S. V. Maleyev, A. I. Okorokov, Y. O. Chetverikov, P. Böni, R. Georgii, D. Lamago, H. Eckerlebe, and K. Pranzas, "Magnetic structure of mnsi under an applied field probed by polarized small-angle neutron scattering," Phys. Rev. B **74**, 214414 (2006).